Environmental Science Nano

Photocatalyzed Electron Exchange between Organic Chromophores and Hematite Nanoparticles and the Role of Solid-State Charge Transport

Journal:	*Environmental Science: Nano*
Manuscript ID	EN-ART-06-2022-000567.R1
Article Type:	Paper

Photocatalyzed Electron Exchange between Organic Chromophores and Hematite Nanoparticles and the Role of Solid-State Charge Transport

Mavis D. Boamah, Xiaopeng Huang, Alan Joly, Zheming Wang, and Kevin M. Rosso

Pacific Northwest National Lab, Physical and Computational Sciences Directorate, Richland, WA 99354.

Corresponding authors: kevin.rosso@pnnl.gov, mavis.boamah@pnnl.gov

Environmental Significance Statement

Electron transfer processes controlling photoreductive dissolution at mineral/organic solution interfaces that lies at the heart of nutrient availability and contaminant transport are challenging to probe due to their ultrafast timescales. Using hematite and a common photoactive dye molecule (rhodamine B) to mimic the effect of chromophoric organic matter sensitization to light-induced charge transfer, we observe a substantially longer dye fluorescence lifetime when adsorbed on hematite nanoparticles with ultrafast transient absorption spectroscopy. Consistent with electron transfer to the oxide, we then explore the influence of pH on the recombination kinetics. We conclude that photoreductive dissolution rates may depend mainly on the physicochemical nature of the mineral particles and photon flux but rely less on the composition of surrounding aqueous solution, especially in the euphotic zone of natural aquatic systems where iron oxide nanoparticles coated with organics exist. This work will shape the direction of basic science research addressing clean energy and water sustainability challenges with nano-mineral-based devices.

Photocatalyzed Electron Exchange between Organic Chromophores and Hematite Nanoparticles and the Role of Solid-State Charge Transport

Mavis D. Boamah, Xiaopeng Huang, Alan Joly, Zheming Wang, and Kevin M. Rosso

Pacific Northwest National Lab, Physical and Computational Sciences Directorate, Richland, WA 99354.

Corresponding authors: kevin.rosso@pnnl.gov, mavis.boamah@pnnl.gov

Abstract

Understanding photocatalyzed redox interactions between Fe(III)-(oxyhydr)oxide mineral nanoparticles and adsorbed chromophoric organic matter is critical for accurately predicting bioavailable iron fluxes in the euphotic zone of natural aquatic systems, and for improving the effectiveness of nano-iron-based water purification systems. However, the electron transfer processes that underpin photoreductive dissolution at particle/organic/solution interfaces occur on ultrafast timescales and thus remain difficult to probe. Here we report an ultrafast transient absorption spectroscopy (TAS) study of suspensions of hematite nanoplatelets (HNPs) sensitized by adsorbed rhodamine B (RhB) dye as a function of solution media and pH. The TAS results indicate a substantially longer fluorescence lifetime of RhB adsorbed on HNPs across a wide range of pH conditions, consistent with transient photoinduced electron transfer to the oxide with recombination kinetics controlled by electron migration back to the interface via small polaron hopping. Normalization of the observed kinetics to the measured surface loading of RhB at different pH values shows that the recombination rates are insensitive to environmental variables, likely controlled instead by particle properties that determine small polaron diffusion behavior.

1. Introduction

In the euphotic zone of natural aquatic systems, photoexcitation at complex interfaces between semiconducting metal oxide nanoparticles, sorbed organics, and aqueous solutions control the bioavailability of important metals such as Cu,[1] Fe,[2] and Mn[3]. Hematite (a-Fe_2O_3) nanoparticles are some of the most common due to the preponderance of iron in host rocks that ultimately weather to yield highly stable secondary mineral iron oxide particulates. With a band gap of ~ 2.2 eV, hematite is photoactive in the near-UV portion of the solar spectrum (l<560 nm).[4-8] In addition to acting as a photocatalytic substrate in natural systems, these traits also enable a variety of electrochemical, magnetic, and optical applications.[9-14] Photoexcitation of these particles can convert a fraction of relatively insoluble Fe(III) in the structure to relatively soluble Fe(II). The efficiency of this photoreductive dissolution process is typically enhanced by common organic acids that sorb to and act as photosensitizers on hematite surfaces.[15-18] By driving Fe(II)/Fe(III) redox cycling, such processes not only affect iron bioavailability[19-22] but also contribute to carbon cycling by transforming sorbed organic matter, either by direct photolysis[23, 24] or by reaction with intermediate reactive oxygen species.[25-32]

Despite being well studied in laboratory experiments[33-36], the mechanism of hematite photoreductive dissolution remains poorly understood because the efficiencies of the various possible light-induced reaction channels remain unknown. At hematite surfaces complexed by organics, two channels to Fe(II) production are possible. Direct photoexcitation of electron-hole pairs that localize to the interface can oxidize bound organics (holes) and produce Fe(II) (electrons). Alternatively, bound organics themselves can act as the chromophores that transfer electrons to Fe(III) in hematite, which then either back-react with the photoexcited organics or release Fe(II). Many factors complicate the experimental goal of unraveling the quantum yields of these reaction channels, including their identical dependence on the concentration of organic surface complexes, and the prospect of parallel organic degradation reactions mediated by consequential production of reactive oxygen species.[37]

Time-resolved experimental studies have steadily emerged that have begun to quantify the interfacial photocatalyzed electron transfer efficiency from bound organic chromophores to Fe(III)-

(oxyhydr)oxide particles, examining the various relaxation channels and the role of environmental variables. In these materials, electrons donated to the conduction band localize by self-trapping and have finite mobilities arising from thermally promoted small polaron hopping.[38-43] Katz et al.,[44, 45] used ultrafast transient absorption spectroscopy (TAS) and time-resolved X-ray absorption spectroscopy (XAS) at the Fe K-edge to monitor dye photoexcitation and injected electron dynamics, respectively, using various Fe(III)-(oxyhydr)oxide nanoparticles sensitized by 2',7'-dichlorofluorescein (DCF) dye at pH 4. Their findings revealed biphasic decay kinetics, the fast domain of which affirmed the small polaron[38-43] model by demonstrating injected electron hopping rates on a sub-nanosecond timescale, followed by a microsecond regime of residual itinerant electron loss. Near the interface, charge carrier migration can be biased by the internal electric fields associated with the space charge layer and pH-dependent surface charge.[46] For example, because hematite often displays n-type semiconduction, band bending usually entails a depletion layer that favors electron migration into interiors while holes accumulate at the interface. Effects of pH conceptually include modifying this field through its control of the surface electrostatic potential; lower pH makes the conduction band minimum a more electrochemically positive and accessible electron acceptor, favoring electron trapping at the interface.[47] pH effects later explored by Soltis et al.[48] using atomistic simulations, which qualitatively recovered the biphasic decay kinetics, suggested a small but significant pH effect on the migration dynamics of injected electrons. However, such effects did not manifest in rates of electron recombination with bound dye molecules as monitored by partner TAS experiments, at least across the pH range 2.9-5.5.

The present study builds on this knowledge by examining a broader pH range, the effects of solvent type and particle loading, and by focusing on structurally well-defined hematite nanoplatelets (HNPs) of uniform size, facet expression, and aspect ratio (90 nm wide by 13 nm thick).[37] Similar to previous work, we employed time-resolved pump-probe TAS techniques to study the photoexcitation dynamics of dye-sensitized particles.[44, 45, 48-51,33] However, in our case, the probe organic species selected was rhodamine B (RhB), a xanthene fluorescein dye. It is used as tracer dye to show the direction and rate of flow and transport. For example, it is often mixed with herbicides to indicate where the herbicide has been applied

easily.[52] Although RhB is not commonly found in geochemical environments, we utilized it as a probe organic because it is well characterized experimentally and theoretically for its transient absorption and excited-state dynamics behavior.[53-60] Because it is chemically stable and undergoes highly reversible photoexcitation under suitable conditions,[55, 57, 59, 61-63] RhB enabled us to focus on the dye relaxation lifetime as a proxy for interfacial electron transfer processes without the interference of simultaneous photodegradation. Furthermore, the pH-dependent speciation of RhB is well known and compatible with the pH-dependent electrostatics of hematite surfaces over a wide pH range, enabling more insight into the role of interfacial electrostatics than in prior work.

We also examine the role of the solvent in our system, which can influence dye binding and relaxation behavior. RhB is known to have longer fluorescence lifetimes in alcohol solvents than in water.[55, 57, 59, 61] Water molecules readily solvate the carboxyl group of RhB dye molecules, thereby lessening its interaction with the xanthene ring. Consequently, the efficiency of nonradiative decay is increased, which shortens the fluorescence lifetime of RhB in water.[59] In an alcohol solvent, hydrogen bond contributions stabilize the positive charge on RhB's amino group. In addition to the higher viscosity of some alcohol solvents, this stabilization reduces internal conversion via motion inhibition leading to longer fluorescence lifetimes.[59, 64, 65] Given that much is known about RhB fluorescence behavior in alcohols versus water, we designed our study to compare RhB/HNP photodynamics in both solvents. Because the excited state lifetime of rhodamine B is independent of concentration below 10^{-4} M in both methanol and water,[55, 62] we choose to perform our work in the micromolar regime. Also, taking a cue from the concentration ratio of dye to nanoparticles used in the previous time-resolved TAS work by Soltis et al.[48], we decided to focus on HNP loadings in suspension at 0.1 or 0.2 g/L.

Comparison of the measured TA behavior of pure RhB solutions, HNP suspensions, and their binary mixtures as a function of particle loading and pH revealed clear evidence for electron injection into HNPs; under select conditions, we find that photoexcitation of RhB is longer-lived when bound to HNP surfaces, consistent with electron injection into the HNPs that delays the back electron transfer reaction and corresponding relaxation of the adsorbed dye. The findings help shed new light on factors controlling the

interplay between photoexcitation of chromophoric organics on metal oxide particles, their semiconducting properties, and the influence of important environmental variables such as pH. The findings are also relevant to conceptually similar research objectives in developing dye-sensitized photovoltaic devices for light-to-electrical energy conversion. For example, previous work demonstrated the importance of quantifying injected electron signals in titanium oxide nanoparticles over microseconds, ultimately to help understand the interfacial electron transfer mechanisms that govern the device performance in nanocrystalline electrodes.[66] This research direction is thus part of a larger scope of basic science directed at addressing clean energy and water sustainability challenges.[33, 67-69]

2. Materials and Methods

2.1 Sample Preparation and Data Collection

Chemicals and Hematite Nanoplatelet Synthesis. Rhodamine B dye (Part No. R6626-25G, Lot# SLBR4051V) and methanol (Lot# SHBL2010, ≥99.9% pure) were purchased from Sigma Aldrich. Deionized water with a resistivity of 18.2 MΩ·cm was used for preparing all water-based dye solutions and HNPs suspensions. The RhB solutions in methanol and water spontaneously yield a pH of ~ 6.7, whereas the HNP suspensions yield a pH of 3 via the buffering capacity of the particles themselves. To achieve the desired pH other than the spontaneous ones, microliter droplets (< 50 µL) of ~ 1 M HCl were added to RhB dye to achieve pH values below 6.7 (i.e., pH 4.5). For all other RhB dye solutions, microliter droplets (~1 – 100 µL) of ~2 M NaOH were added to achieve the desired pH above 6.7. Likewise, for hematite nanoparticle suspensions, microliter droplets (~5 – 100 µL) of ~2 M NaOH were added to reach pH 4.5, 7, 9, and 11 before adding them to RhB dye. Between RhB dye and RhB/HNPs samples, we allowed pH variation of ±0.25 for pH 9 and 11 experiments. For pH 4.5 and 7 experiments, we allowed pH variation of ±0.1.

Hematite nanoplates dominated by the (001) facet were synthesized following the previously outlined procedure in a publication by Huang et al.[37] Briefly, following the dissolution of 1.09 g of iron (III) chloride hexahydrate (Fisher Chemical, Lot# 189115A) in 40 mL ethanol (Deconlabs, Lot#

A11011904T.) with 2.8 mL deionized water, 3.2 g of sodium acetate (AMRESCO, ACS Grade, Lot#. 2105C458) was added to the mixture.[70] Subsequently, 100 mL of the mixture transferred to a Teflon-lined stainless-steel autoclave was heated at 180℃ for 12 hours.[70] After cooling to room temperature, precipitation from the mixture was collected and rinsed with water and ethanol. The precipitate was dried in a desiccator at 40℃ for 12 hours.[70]

All experiments were performed with 65 μM and 20 μM RhB dye dissolved in water or methanol. The effective mass loadings for hematite nanoparticles were kept at 0.1g/L and 0.2 g/L for all suspensions. Each RhB dye and HNPs suspension was hand-swirled for at least 10 minutes before TAS measurements.

Time-Resolved Transient Absorption Spectroscopy. TAS measurements were performed using the instrument currently in EMSL at Pacific Northwest National Laboratory (PNNL), which is composed of a 1kHz regeneratively amplified Ti:sapphire laser system (Legend Elite DUO, Coherent, Inc.) with sub-40 fs pulse width and total power output of ~ 7.6 W at 800 nm, integrated with a commercial transient absorption spectrometer (TAS system, Newport). In this setup, ~ 2.5 W of the 800 nm output from the Ti:sapphire laser is used to pump an optical parametric amplifier with difference frequency generation (OPA-DFG OPerA-Solo, Coherent, Inc.) to generate a pulse with a wavelength between 515-520 nm serving as the pump pulse of the spectrometer. For all our experiments, the pump beam power immediately before the sample stage in the spectrometer was held at 0.35 ± 0.05 mW. Neutral density filter and chopper regulated the pump power before hitting the sample. About 1.0 W of the 800 nm output is directed from the Ti:sapphire laser into the transient absorption spectrometer through an automated beam steering system (Newport) controlled by the Newport ABS software. A part of the 800 nm beam is fed into a four-pass Newport retroreflector mounted on a Newport delay stage with 4.3 ns total travel and 1 fs standard step size and is used for white light generation with a CaF_2 crystal (350 nm – 700 nm) within the spectrometer. The white light intensity was adjusted with a variable optical density filter wheel. The time delay between the pump pulse and probe pulse is determined by moving the position of the retroreflector on the delay stage. The transient signal (change in optical density, ΔOD) was calculated based on the difference between the white light intensity with and without the pump beam by the Time-Resolved Spectrometer software

(Newport, version 2). The suspension samples were placed in quartz cuvettes of 2 mm optical path length (Type 21-Q-2, Starna Cells). The cuvettes were mounted on an X-Z translation stage that constantly moved in a spiral pattern to avoid localized sample heating. For better data fidelity, we undertook at least triplicate TAS measurements of RhB dye with or without HNPs for each pH and/or solvent.

UV-Vis Experiments. UV-Vis measurements were carried out to quantify the amount of rhodamine B (RhB) sorbed onto HNPs in suspension. First, we recorded the UV-Vis spectrum of either 65 μM and 20 μM RhB dye only in either water or methanol. We then added a predetermined amount of HNPs to 10 mL of RhB solutions to achieve a final loading of either 0.1 g/L or 0.2g/L of HNPs and a concentration of 65 μM or 20 μM RhB. The RhB dye and HNPs suspensions were hand-swirled for at least 10 minutes before taking a UV-Vis spectrum. To eliminate the background absorption of the HNPs from the estimation, we took UV-Vis spectra of 0.1 g/L and 0.2 g/L HNPs suspended in either water or methanol after 10 minutes of agitation. All measurements were performed at least in duplicates for each combination of dye concentration, HNPs loadings, and pH studied.

2.2 Data Analysis

Transient Absorption Spectroscopy. Singular value decomposition-based global analyses were conducted for the TAS data using Glotaran Software package. Glotaran is a Java-based graphical user interface to the R package TIMP.[71] It enables fitting superposition models to multidimensional data obtained from time-resolved spectroscopy. Glotaran allows the decomposed data to track the distribution of the rate constants as dependent on wavelength. Singular value decomposition[71] estimates the number of independent events in the TAS data. We employed a three-component decay model for TA data decomposition for RhB only solutions and RhB with hematite nanoparticle suspensions.

Stretched Biexponential Fitting for Transient Absorption Kinetics. The Glotaran global fits returned three different excited-state relaxation time values, as discussed above. Many systems, including ultrafast electron transfer phenomena, exhibit a stretched exponential behavior, which describes the recorded kinetics as a sum of exponential decay processes with varied relaxation time constants. As a result, we could safely describe the transient absorption peak centered around ~448 nm as a triexponential decay

process, $\Delta OD(t) = A_1 e^{-\left\{\frac{t}{\tau_1}\right\}} + A_2 e^{-\left\{\frac{t}{\tau_2}\right\}} + A_3 e^{-\left\{\frac{t}{\tau_3}\right\}}$.[72] Here, τ_1 is the first excited state relaxation time related to the excited state decay of RhB's dimer, τ_2 is the fluorescence lifetime, τ_3 is the third excited state relaxation lifetime, ΔOD is the change in optical density or transient absorption signal, t is the delay position, A_1, A_2, and A_3 are amplitude factors. τ_3 values are larger than the delay position(t) and τ_2 (*vide infra*). Thus, $A_3 e^{-\left\{\frac{t}{\tau_3}\right\}}$ can be treated as constant, since $\frac{t}{\tau_3}$ approaches zero. To separate the pH-dependence of RhB's fluorescence from the influence of RhB sorption extent on its excited-state relaxation time, we adopted the stretched exponential methodology and paid attention to both the RhB dimer's excited state lifetime - τ_1 and fluorescence lifetime - τ_2 to adequately describe the change in decay patterns recorded at 448 nm after RhB's sorption onto HNPs.[48, 72-74] The stretched exponential enables us to account for RhB's pH-dependent (i.e., its molecular state driven) fluorescence lifetime to retrieve solely the change in fluorescence lifetime driven by RhB's sorption onto HNPs. Transient absorption kinetic curves for RhB+HNPs observed at 448 nm were fitted to the stretched biexponential equation expressed as $\Delta OD(t) = A_1 e^{-\left\{\frac{t}{\tau_1}\right\}^{\propto}} + A_2 e^{-\left\{\frac{t}{\tau_2}\right\}^{\beta}} + \Delta OD_0$**,** in Igor Pro (version 8.02 64-bit) with fixed time constants - [τ_1, τ_2] to retrieve the stretching factors - [α, β] associated with τ_1 and τ_2, respectively to assess RhB's fluorescence when sorbed onto HNPs.

UV-Vis. To determine the amount of RhB sorbed onto the HNPs, the baseline for the RhB and HNPs suspension (RhB+HNPs) spectra were first corrected for absorption by HNPs only. Next, the peak height of RhB+ HNPs suspension was subtracted from the peak height of RhB only to obtain the change in absorbance. The peak absorbance change is converted to concentration using Beer's Law. To calculate the micromoles of RhB sorbed per meter square of hematite nanoparticles, the following equation was utilized: $C_S = \frac{[C_i - C_e]V}{M_S A}$, where C_S ($\frac{\mu mol}{m^2}$) represents the amount of dye sorbed onto the HNPs, C_i($\frac{\mu mol}{L}$) is the initial concentration of RhB right before any sorption occurs, C_e($\frac{\mu mol}{L}$) is the concentration of RhB in suspension with HNPs at equilibrium, V (L) is the volume of the suspension, A($\frac{m^2}{g}$) represents the specific

surface area of the HNPs, and $M_s(g)$ is the mass of HNPs.[75, 76] Using a density of 5.28 g/cm³ based on the hematite unit cell and surface area of 20880 nm² per HNP, A was calculated as 37.56 m²/g.

3. Results and Discussion

3.1 Sorption of Rhodamine B onto Hematite Nanoparticles

We collected UV-Vis measurements of RhB mixtures before and after adding HNPs to estimate the amount of RhB dye sorbed onto HNPs at different RhB concentrations, HNP loadings, and at our various pH values in methanol and water. In the absence of pH titration, initial HNP suspensions naturally equilibrated to pH ~3 in both water and methanol due to the natural buffering capacity of the nanoplatelets. Thus, unless otherwise noted, the selected experimental pH values of 4.5, 7, 9, and 11 discussed below were achieved using pH titration (see Methods).

The molecular structure of RhB consists of three benzene rings, two N-ethyl groups, one phenoxy, and one carboxyl group (Scheme 1). RhB can speciate as cation, zwitterion, or lactone forms.[61, 77, 78] In water, the cation form exists below pH 7, whereas the zwitterion exists above pH 7.[79-81] The lactone, a neutral molecule, exists mainly in non-polar and aprotic solvents.[79-81] Since our work here involves only polar and protic solvents; we have only the cation and zwitterion forms in play (Scheme 1). The carboxyl group possesses two electronegative oxygen atoms doubly bonded to a carbon atom, thus contributing to a lower electronegativity within the RhB molecule. Therefore, it is expected that the carboxyl group will most likely coordinate with iron hydroxy cations to form the iron oxide-RhB surface complex. Indeed a DFT calculation confirmed that stable monodentate Fe-RhB surface complexes on hematite are formed via the -COOH groups.[82] Given that water strongly solvates the -COOH of RhB, it has the potential to more strongly influence its binding to the HNPs than methanol.[59, 64, 65] Nonetheless, we did not observe any significant

differences between the amount of RhB sorbed onto HNPs in water versus methanol at a given pH and an initial RhB concentration (Tables S1-S2).

The pH-dependent speciation and chemical behavior in our system in water and methanol are taken to be approximately similar. For example, the equilibrium pH when RhB solutions and HNP suspensions are combined yields pH ~3 in both solvents (Table S1). UV-Vis-based estimation shows that the amount of RhB sorbed by HNPs in methanol increases in the order pH 4.5 < pH 11 < pH 7 ~ pH 9 (Fig. 1, Table 1). HNPs sorbed more dye at an initial concentration of 65 μM than at 20 μM in both methanol and water (Tables S1-S2), consistent with the higher chemical potential of RhB in 65 μM solutions.

The observed sorption behavior of RhB on the HNPs at various pH values is generally consistent with the pH-dependent speciation of RhB as well as the expected surface charging behavior of hematite. In water, the point of zero net charge of the dominant (001) face of our hematite nanoplatelets should be between pH 8 – 9 in the case of perfect single crystals, but can be as low as 6 on powders, reflecting its strong dependence on surface defects and preparation method.[83-86] The pKa of RhB dye is ~ 6.41, so at pH 4.2, its aromatic carboxylic group is fully protonated as -COOH.[75, 78, 87-90] Therefore, at pH 4.5, because the RhB cation dominates the solution speciation and HNPs are net positively charged, the observed RhB sorption suggests that hydrogen bonding can outcompete electrostatic repulsion. At and above pH 7, RhB speciation is dominated by its zwitterion form, and the HNP's are slightly positively charged to charge neutral. Hence the zwitterion form of RhB can bind electrostatically via its negatively charged carboxyl group, as well as by hydrogen bonding. At pH 9, where the HNPs are effectively neutral to slightly negatively charged, binding with the zwitterion form of RhB can occur by hydrogen bonding and mild electrostatic attraction. Finally, at pH 11, where the HNPs are net negatively charged, in addition to hydrogen bonding, electrostatic attraction with the RhB zwitterion can be facilitated by its positively charged group, thus in this case likely involving a different molecular orientation of RhB on the HNP surface. Hence, over our experimental pH range generally, RhB adsorption capacity is expectedly highest at pH 7 and 9 and lowest at pH 4 and 11. Indeed, our UV-Vis-based estimation of the concentration of dye sorbed by HNPs at varying pH values reflects these predictions (see Table 1, Fig. 1D, and Table S2).

Because of the qualitative similarities in the pH-dependent behavior in both water and methanol, we assume that the presented basis for RhB sorption is largely the same in both solvents.

3.2 Transient Absorption of Rhodamine B in Methanol and Water

Transient absorption curves of 65 µM RhB in methanol were recorded at pH values ranging from 4.5 to 11 (Figs. 2-5, grey-scale curves only). Additional TAS experiments were conducted for 20 µM and 65 µM of RhB dissolved in either water or methanol at pH 11 and the unadjusted or natural pH value of ~ 6.7 (see SI, Figs. S1-S8, grey-scale curves only). From ~380 nm – 470 nm, transient absorption peaks with maximum positive ΔOD around ~ 445 nm - 450 nm were observed for the RhB dye. Ground-state bleaching and stimulated emission peaks are centered at ~ 510 nm and ~ 560 nm, respectively (Figs 2-5, Figs. S1-S8).

Based on Glotaran global analysis, we retrieved three excited state relaxation time(s) for 65 µM and 20 µM dye concentrations at varying pH values (Table 2). The first relaxation time spans from ~3 ps - 100 ps, the second relaxation time spans from ~ 0.6 ns - 2.3 ns below pH 9 but up to ~ 6 ns at pH 11, and the third relaxation time spans from ~ 5 ns – 0.1 µs. Previous work has shown that the excited state decay of RhB's dimer dye takes place within 100 picoseconds in water, showing good correspondence with our fastest measured relaxation time.[91] Vazquez et al. reported that the fluorescence decay of RhB occurs at ~1 ns based on quantum chemical simulation.[56] Indeed, several studies of RhB fluorescence ($S_1 - S_0$) have affirmed the lifetime to be on the order of a few nanoseconds, in good correspondence with our second measured relaxation time.[55, 57-60] Finally, Vazquez et al. indicated that RhB's intersystem crossing ($S_1 - T_2$) and reverse ($T_1 - S_1$) occur within micro-and hundreds of seconds.[56] Intersystem crossing studies of RhB in ethanol also reported a lifetime of 6 µs.[92] Based on these findings; we can deduce that the first excited state relaxation time ($\boldsymbol{\tau_1}$) from the global analysis describes the excited state decay of RhB's dimer. The second excited state relaxation time ($\boldsymbol{\tau_2}$) is from the fluorescence process. The third relaxation time ($\boldsymbol{\tau_3}$) likely relates to intersystem crossing.[55-57, 91, 92]

Also consistent with the previously reported observations for both zwitterion and cation forms of RhB,[55, 57, 61] we observe that the fluorescence decay of RhB dye occurs faster in water than in methanol (Table 2). For example, at pH 11, where the zwitterion dominates, the stronger solvation of the COO^- group

by water reduces its strength of interaction with the xanthene ring leading to an increase in nonradiative decay and a decrease in the fluorescence lifetime.[55, 57, 59, 61] However, unbuffered RhB solutions at 20 and 65 µM concentration show a slow acidic drift from pH 6.7 to pH 6.5 and down to pH 6 within ~30 and 120 minutes, respectively, both in water and methanol when left unperturbed with no laser introduction. Here, within the first hour of solution preparation, we observed that the fluorescence occurs faster in methanol than in water for 20 µM RhB, whereas for 65µM RhB's fluorescence lifetimes are roughly the same in both water and methanol. This appears to contradict what was reported by Magde et al.[59] for near-neutral solutions of ≥ 2 µM RhB in both water and organic alcohols, but they did not state if their solutions were buffered or not. Zhang et al.[57] acknowledged that an acid-base equilibrium exists for RhB solutions in protic solvents. Therefore, they prepared their rhodamine B dye solutions with water or alcohol that contained 1 mM NaOH to keep the pH constant (~ pH 11) for their fluorescence studies. In our case, we speculate that the reverse fluorescence lifetime trend for unbuffered RhB solutions in water versus methanol for 20 µM RhB arises from the changing equilibrium concentrations of the different forms of RhB dye at its natural state because no buffer was added to stabilize the dye solutions (see Table S3).

Our τ_2 values obtained from Glotaran analysis show that pH influences the fluorescence process of RhB. In methanol τ_2 ranks as follows: pH 11 > pH 4.5 > pH 7 ~ pH 9. The cation molecular form is dominant at pH 4.5, and the zwitterion molecular form is dominant at the remaining pH values. If we account for the dye's molecular state and set aside the pH 4.5 value, the remaining values suggest an increase in τ_2 with increasing pH to 11. Previous work in the literature investigated the fluorescence lifetime(s) of the zwitterion and cation forms of RhB in water and alcohol solvents.[59, 61] Although they did not explicitly discuss respective fluorescence lifetimes, their data suggest that the zwitterion fluorescence is longer. Nonetheless, the differences in fluorescence lifetime(s) reported for the two forms in water, ethanol, and other organic solvents are not statistically significant. Only Magde et al. mentioned that they obtained the cation form by adding chloroacetic acid to the RhB solution. Still, it remains unclear in those

studies if the zwitterion or cation form was dominant in their experiments since they did not report pH values of the RhB dye solutions.[59, 61]

3.3 Transient Absorption of the RhB/Hematite system.

Given knowledge of the photoexcitation processes occurring in pure RhB solutions, we then examined how these processes change when mixed with HNP suspensions. Our main hypothesis is that photoexcitation of adsorbed RhB can, under certain conditions, couple to the electronic structure of hematite by electron transfer into its conduction band from RhB in its excited state. This is conceptually supported by the clear overlap between the optical absorption of RhB and HNPs (Fig. 1A and 1C).

Pure Hematite Nanoparticle Suspensions. To do this first required control TAS measurements on pure HNP suspensions. For these measurements, to facilitate comparison to previous work[50, 93, 94], we focused on water as the solvent, without pH buffering, and HNPs loading of 1 g/L. Fitting the decay data for the HNPs suspensions in water to a biexponential curve at 600 nm yielded averaged excited-state relaxation time values of 98 ± 30 ps and 1018 ± 501 ps (see SI, Text S2). These values are reasonably close to the inter-band charge carrier recombination time(s) (>100 ps) reported in prior studies on hematite in air and water.[50, 93-96] Specifically, TAS studies of hematite nanofilms in air yielded two excited-state relaxation time values of 5.7 ps and > 670 ps after fitting kinetic curves recorded at 579 nm (2.14 eV).[97] Recombination of relaxed electrons (i.e., fully relaxed hot electrons in the lower conduction band of hematite) with holes accounts for the longer lifetime values retrieved.[50, 93, 97, 98] Based on the similar timescales with RhB fluorescence, one would expect electrons transferred from photoexcited RhB adsorbed on the surface to prospectively intermeddle with the direct band gap photoexcitation of hematite by filling photogenerated holes in the valence bands.[44, 45, 48, 50, 55, 57-59, 61,93, 97-99] Indeed, previous studies have shown that while some electrons transferred from photoexcited dichlorofluorescein dye into iron oxide return within ~ 3 ns, a significant residual proportion of the injected electrons remain for at least 1 μs.[44, 45, 48, 99] Thus, we can expect electron transfer from photoexcited RhB into hematite to interfere mainly with the fluorescence and, to a certain degree, the intersystem crossing of the RhB molecule. Indeed, as discussed below, our TAS results

regarding relaxation lifetime values for RhB in suspension with HNPs reflect these expectations, especially for pH values at or below the pH range for surface charge neutrality on hematite.

RhB/Hematite at Acidic Conditions. We added HNPs in their naturally acidic suspensions to RhB dye solutions forming RhB/HNP mixtures in either water or methanol and, after sorption equilibrium was attained, performed TAS measurements in these acidic suspensions (equilibrated pH of ~3 in both methanol and water) (Table S1, Table S3). HNPs loadings were set to 0.1 g/L and 0.2 g/L for 65 μM and 20 μM initial concentrations, respectively, for both solvents. Figures S1-S4 show transient absorption and kinetics curves recorded at 448 nm for RhB and RhB+HNPs at the natural pH. The transient absorption spectra display peaks at a few chosen delay positions (Top parts, Figs. S1-S4).

The fluorescence lifetime, τ_2, increases by at least 50% after equilibration with the HNPs, but only in methanol and not in water (Table S3). In contrast, in water, τ_2 decreases by ~30% and 60% for 20 μM and 65 μM RhB after HNPs are added. Because we can attribute delayed fluorescence to electron transfer from sorbed RhB to hematite, the finding suggests that the stronger interaction between water and the carboxyl group of RhB that accelerates its fluorescence relative to that in methanol becomes enhanced in the presence of HNPs. This acceleration is consistent with the notion that HNP surfaces provide water and hydroxylated functional groups that can solvate the carboxyl group of RhB, yielding a similar effect as that of bulk water molecules, thereby decreasing its propensity for interfacial electron transfer.[59, 64, 65] In methanol, however, because the OH bond of CH_3OH donates to RhB's amino nitrogen atom to stabilize the amino substituent's positive charge, this weakens the solvation of the phenyl-COOH.[59, 64, 65] A consequence is the likelihood of a more intimate association of RhB with HNP surfaces and promotion of the interfacial electron transfer process. Hence, for the purposes of evaluating the effect of pH on the interfacial electron transfer process in more detail, we choose to focus exclusively on experiments performed in methanol.

RhB/Hematite at Alkaline Conditions. To compare with the acidic system behavior, we focus here on pH 11 conditions in methanol, where the zwitterion dominates, and the net surface charge of the HNP's can be safely assumed to be negative. Figures S5-S8 display transient absorption and kinetics curves recorded at 448 nm for RhB and RhB+HNPs at pH 11. The transient absorption spectra reveal peaks for a few delay

positions (Top parts, Figs. S5-S8). Here we observe consistent decreases ($\geq$ 9%) in τ_2 -the fluorescence lifetime at pH 11 when RhB and RhB+HNPs samples are compared (Table S4). Importantly, this effect is relatively constant when the solvent is changed to water, or when RhB concentration or HNP loading is changed (see SI, Tables S3-S4). The effect is similar to that observed at acidic conditions in water, in that introduction of the HNPs appears to accelerate the fluorescence through the presentation of hydrated/hydroxylated surface functional groups that can solvate the carboxyl group of RhB.[59, 64, 65] However, in this case, we must also consider the prospect of a change in net surface charge impacting RhB binding and surface complexation, particularly because we observe that more RhB sorbs at alkaline rather than acidic conditions (Table 1). The change in net surface charge from positive to negative would tend to favor reorientation of the RhB zwitterion to bind preferentially through its positively charged amino groups rather than its carboxyl group. Because our data do not provide a basis for ruling either effect out, future work on this open question would be useful.

RhB/Hematite at pH 4.5 to 11. Given that we observed no dependence of electron transfer from RhB to HNPs on RhB concentration or loading of HNPs; we performed TAS studies of 65 μM RhB dye in 0.1 g/L HNP suspensions in methanol over a range of titrated pH values to explore the pH effect more systematically. Figures 2-5 display representative TA spectra and kinetics data for RhB and RhB+HNPs samples at pH 4.5, 7, 9, and 11. The spectra show peaks at specific delay positions (Top parts of Figs. 2-5). The fluctuations evident in the raw TA kinetics data initially appeared to depend on pH, with increasing fluctuations as pH decreased. To determine if this carried information specific to the HNP/RhB interface we normalized ΔOD RhB+HNPs to that of RhB alone at each pH for all delay positions (Fig. S9). The graphed ΔOD difference data removes this dependence, suggesting that the observed trend in fluctuations, if meaningful, relates to the pH dependent speciation of RhB.

The raw TA kinetics data at 448 nm is well described by biexponential decay equations involving τ_1 and τ_2 (see data analysis), which depict that RhB+HNPs suspensions relax slower than otherwise identical pure RhB solutions (Figs. 2-4), except at pH 11 (Fig. 5), which may be due to the stated different binding mode of RhB on net negatively charged surfaces. At the same time, τ_1 values barely change when RhB and

RhB+HNPs are compared (Table 3, Fig 6A), suggesting no effect of sorption on the decay process of RhB's dimer. We thus focus on the observed systematic increase in the fluorescence lifetime across pH 4.5, 7, and 9 (Table 3, Fig. 6B), where τ_2-values rise by ~68%, 99%, and 101%, respectively (Fig. 6B). The observed systematic increase in the fluorescence relaxation lifetime with increasing pH could suggest a relationship between the efficiency of the interfacial electron transfer and the molecular details of RhB binding to the HNP surfaces and/or the residence time of injected electrons, both of which could, in turn, be controlled by the net surface charge on the particles. At pH 4.5, the surface charge is positive, a condition that has been shown to trap injected electrons in the near-surface region of iron oxide particles,[46, 48] facilitating their back-reaction to acceptors at the surface, in this case photoexcited RhB molecules. At the more net neutral surface charge conditions at pH 7 and 9, injected electrons explore interior sites.[46, 48] Because their escape back to the surface follows a random walk less biased by the net surface charge, the back-reaction electron transfer rate can be slower, and the consequence would be a longer RhB fluorescence lifetime. The corresponding delay consistent with what we observe in our τ_2 results would be on the order of a few nanoseconds.

However, because pH also controls RhB speciation and its surface loading on the HNPs (e.g., Table 1), it was necessary to attempt to normalize our τ_2 values to the measured surface RhB concentration at each pH to determine if the apparent correlation between pH and τ_2 remains intact. Our global fitting process could not independently account for the pH dependence of RhB fluorescence lifetimes for the RhB+HNP suspensions. Therefore, the fluorescence lifetimes presented so far for the RhB+HNPs suspensions in Table 3 and Figure 6B are convoluted with the possible influence of pH-specific RhB sorption extent. To separate these effects, we had to adopt an exponential decay fitting strategy that will allow us to consider the pH-dependent fluorescence lifetimes of RhB-only in our fitting basis. Thus, we employed a stretched biexponential method (see Materials and Methods) to fit the TA kinetics data seen at 448 nm for pH 4.5, 7, and 9. Given that the third relaxation lifetime of photoexcited RhB dye, τ_3 is greater than τ_2, and τ_3 increases over 100% at pH 7 and 9 but barely changes at pH 4.5 after HNP inclusion (Fig. 6C), it is safe for

us to treat the kinetics measured at 448 nm as biexponential decay because τ_3/delay position(t) approaches zero [$TA\ signal \propto e^{-\left\{\frac{t}{\tau_1}\right\}} + e^{-\left\{\frac{t}{\tau_2}\right\}} + e^{-\left\{\frac{t}{\tau_3}\right\}}$, $where\ e^{-\left\{\frac{t}{\tau_3}\right\}} \rightarrow e^{-0}$]. The stretched biexponential [$TA\ signal \propto e^{-\left\{\frac{t}{\tau_1}\right\}^{\alpha}} + e^{-\left\{\frac{t}{\tau_2}\right\}^{\beta}} + constant$] allows us to directly account for the pH dependency of RhB-only solutions enabling us to delineate the influence of RhB's sorption onto HNPs. Here, we used the τ_1 and τ_2 values obtained from the Glotaran analysis for RhB-only solutions at the respective pH values (Table 3) as fixed time constants to retrieve β, the stretching factor associated with the fluorescence lifetime (see data analysis, Figs. 7A-C). Thus, the value of α, the stretching factor associated with the dimer's excited state lifetime, is set to unity (α = 1) for the three pH values because τ_1 remains the same after the inclusion of HNPs (Fig. 6A). Also, a range of 0 to 1 is set for β as required by the stretched exponential method.[72]

Figure 7D reveals that the resulting β values for pH 4.5-9 are statistically equivalent, indicating that most of the observed pH dependence in the fluorescence lifetimes shown in Figure 6B arises from its effect on the surface concentration of RhB. In principle, this analysis also removes effects arising from the molecular state of RhB, either cation or zwitterion, to the extent that this speciation controls its loading on the surface (i.e., it does not remove any difference in electron transfer propensity that may intrinsically depend on RhB speciation). It also corrects for the surface charge effect, again only to the extent that it affects RhB surface loading and not the surface charge effect on injected electron residence times. Having normalized the loading effects out of the pH-dependent τ_2-values, we obtain a result that is generally consistent with prior precedent – the residence time of electrons injected into the HNPs by photoexcitation of adsorbed RhB tends to stay constant, even as the net surface charge transitions from positive to circumneutral. This finding suggests that other pH-dependent effects on the RhB/HNP photoexcitation system are either negligible or mutually offsetting.

Significance with respect to previous time-resolved experiments and computational work. Zarzycki and Rosso performed molecular dynamics simulations to understand the role of changing surface charge with pH on metal Fe(II) sorption coupled to interfacial electron transfer.[100] They reported that Fe(II) adsorbs via inner sphere complex above the point of zero net charge on the negatively charged Fe(III)-oxyhydroxide

(i.e., goethite) surface but adsorbs via outer sphere complex below the point of zero net charge on the positively charged goethite surface.[100] The inner and outer sphere sorption complexes led to non-adiabatic and adiabatic electron transfer, thus indicating a significant pH-dependent process for metal sorption coupled to interfacial electron transfer.[100] In our work here, we observe no statistically significant pH-dependent effect on the rate of electron recombination with sorbed RhB organic dye on hematite. The work performed here used an organic zwitterion or cation dye as the sorption material, whereas Zarzycki et al. used Fe(II) ions, highly charged species.[100] Charged Fe(II) species would naturally be more sensitive to surface charge changes and interact more strongly via electrostatics with the charged iron oxide surface than bulky organic rhodamine B dye in its cationic or zwitterionic state. Thus, the mode and strength of interaction between Fe(II) and iron oxide surface, which ultimately determines an adiabatic or non-adiabatic electron transfer, will be more highly affected by pH than between bulky organic molecules and iron oxide surface. Indeed, the amount of RhB sorbed onto the iron oxide surface did not differ greatly with pH (Table 1, Fig. 1D).

Previous TAS and time-resolved XAS studies of Fe(III)-(oxyhydr)oxide nanoparticles provided important initial observations of how surface charge, suspension pH, aggregation state, particle size, the energy of the pump beam, and electron mobility influence photo-initiated interfacial electron transfer from bound chlorofluorescein dyes.[44, 45, 48, 99] The seminal study by Katz et al. using time-resolved XAS at the Fe K-edge enabled the concentration and lifetime of electrons injected into hematite, maghemite, and ferrihydrite nanoparticles to be directly monitored, providing clear evidence of biphasic relaxation kinetics that was later supported by atomistic Monte Carlo simulations of collective small polaron electron hopping dynamics in representative ferrihydrite particles by Soltis et al.[48] Those simulations further supported the notion of a small but significant effect of environmental variables such as pH on the electron migration dynamics back to excited dye molecules at particle surfaces. However, because this effect did not manifest in partner TAS measurements of dye relaxation lifetimes, it was concluded that other mechanisms dominate. In particular, the possible overriding importance of deep trap states, such as those associated with defect sites in the material, were highlighted.

Our TAS study, which focused on structurally and chemically well-defined hematite nanoplatelets, and that has examined the widest range of pH to date using a distinct dye RhB, arrived at a similar conclusion. After correcting for the pH-dependent amount of RhB surface loading on the HNPs, we observe no statistically significant pH-dependent effect on the rate of electron recombination with sorbed dye molecules. Injected electron dynamics appear to behave largely independent of chemical conditions that dictate the characteristics of the electrical double layer at the particle/organic/solution interface. Although our work does not directly monitor injected electron mobilities, the work by Katz et al.[44, 45] showing biphasic decay is deemed relevant to the present case. Hence properties of the Fe(III)-(oxyhydr)oxide nanoparticles that control the energy landscape for electron trapping/de-trapping and small polaron mobilities appear to overwhelm surface-specific electrostatic effects. Further complementation of our work by time-resolved XAS studies at the Fe K-edge will be used to examine particle-specific injected electron dynamics directly. Future work must also ultimately seek to understand the influence of the increased system complexity found in real environmental systems, such as structural and compositional defects in the nanoparticulate iron oxides, the role of their various possible phases and facets, immersed in multicomponent aqueous solutions. In particular, such factors are likely to impact the uptake and photo-induced electron transfer behavior of dissolved soil organic matter attached to iron oxide particle surfaces in near-surface aquatic systems.

4. Conclusions

TAS studies of hematite nanoplates sensitized by RhB dye were carried out to examine the effects of environmental factors on the efficiency of photoinduced interfacial electron transfer and relaxation dynamics that control transient Fe(II)/Fe(III) ratios in these particles and, ultimately their photoreductive dissolution rate. Our approach took advantage of well-known distinct excited-state relaxation times for RhB dye assigned to dimer's excited state decay, fluorescence ($S_1 - S_0$), and intersystem crossing ($S_1 - T_2$)

processes[55-58, 60, 91] to link nanosecond fluorescence lifetimes to the propensity of interfacial electron transfer and electron mobilities in HNPs. TAS results for both 65 μM and 20 μM RhB dye showed increases on the order of 50% in fluorescence lifetime when in contact with 0.1 g/L or 0.2 g/L HNPs in methanol across a pH range from mildly acidic to mildly alkaline. The increase in fluorescence lifetime of the RhB+HNPs system is consistent with transfer of electrons generated from the photoexcitation of the sorbed RhB dye to the conduction band of hematite, where trapping as small polarons of limited mobilities delays on nanosecond timescales their return to the interface for recombination with sorbed dye molecules in the excited state. When corrected for the pH-dependent surface loading of RhB, the delay takes on a pH-independent behavior that suggests that particle-specific factors that control electron mobilities outweigh environmental variables that control the electrostatic potential distribution at the particle/organic/solution interfaces. In combination with previous time-resolved work, the findings suggest that in the euphotic zone of natural aquatic systems where Fe(III)-(oxyhydr)oxide nanoparticles coated with organic matter are common, that photoreductive dissolution rates may depend primarily on the physicochemical characteristics of the mineral particles, the photon flux, and the photoexcitation properties of chromophores in the sorbed organic matter, and less on the composition of the surrounding aqueous solution.

Supplementary Information
SI contains text, figures, and tables describing TAS and UV-Vis experimental results obtained for rhodamine B and hematite nanoparticles at pH 11 and unadjusted pH values.

Author Information
Corresponding Authors

Kevin M. Rosso – Physical and Computational Sciences Directorate, Pacific Northwest National Lab, Richland, WA 99354, United States; orcid.org/0000-0002-8474-7720

Mavis D. Boamah – Physical and Computational Sciences Directorate, Pacific Northwest National Lab, Richland, WA 99354, United States; orcid.org/0000-0003-4457-4594

Authors

Xiaopeng Huang – Physical and Computational Sciences Directorate, Pacific Northwest National Lab, Richland, WA 99354, United States; orcid.org/0000-0001-6606-7468

Zheming Wang – Physical and Computational Sciences Directorate, Pacific Northwest National Lab, Richland, WA 99354, United States

Alan Joly – Physical and Computational Sciences Directorate, Pacific Northwest National Lab, Richland, WA 99354, United States; orcid.org/0000-0003-2931-4524

PNNL Release Number: PNNL-SA-174094

Conflict of Interest
The authors declare no conflict of interest.

Acknowledgment
This material is based upon work supported by the U.S. Department of Energy (DOE), Office of Science, Office of Basic Energy Sciences, Chemical Sciences, Geosciences, and Biosciences Division through its Geosciences Program at Pacific Northwest National Laboratory (PNNL). MDB acknowledges support from the Linus Pauling Post-Doctoral Fellowship program at PNNL. A portion of the work was performed using the Environmental and Molecular Sciences Laboratory (EMSL), a national scientific user facility at PNNL sponsored by the DOE's Office of Biological and Environmental Research. PNNL is a multi-program national laboratory operated by Battelle Memorial Institute under contract no. DE-AC05-76RL01830 for the DOE.

Figures and Tables

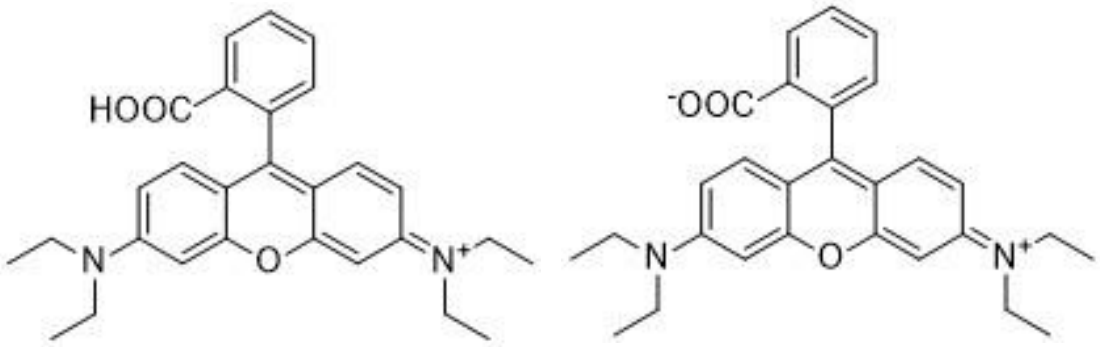

Scheme 1. Chemical structures of (Left) Cation form and (Right) Zwitterion form of rhodamine B.

Solvent	[RhB] [μM]	pH	[HNP] [g/L]	[RhB] sorbed by HNPs [μM]	Sorbed RhB [μmol/m²]
Methanol	65	4.5	0.1	3.19±1.96	0.85±0.52
Methanol	65	7	0.1	12.15 ± 4.57	3.24±1.22
Methanol	65	9	0.1	13.31 ± 7.49	3.54±1.99
Methanol	65	11	0.1	7.14 ± 3.15	1.90±0.84

Table 1. Table showing the amount of rhodamine B sorbed onto hematite nanoparticles at pH 4.5, pH 7, and pH 9 when 0.1 g/L hematite nanoparticles are suspended in 65 μM dissolved in methanol. Error values shown here are based on one standard deviation.

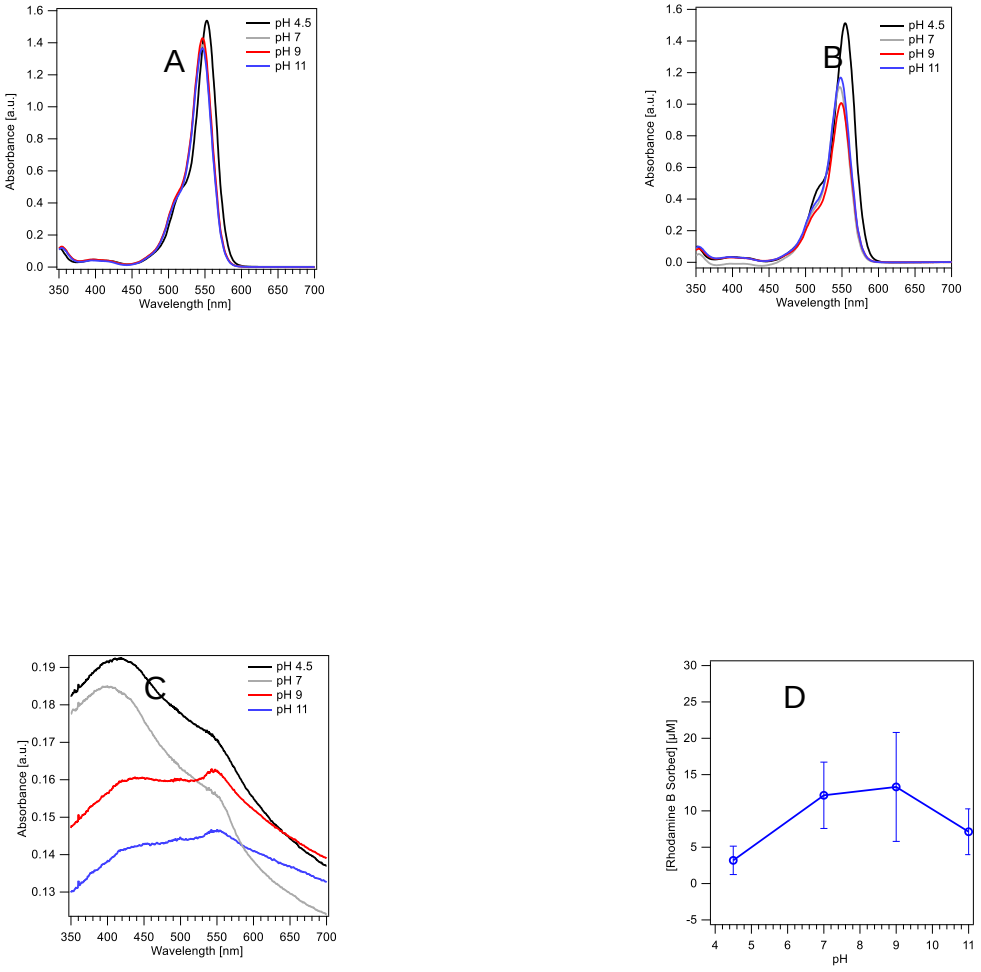

Figure 1. Representative UV-Vis absorption curves recorded at different pH values for (A) 65μM rhodamine B in methanol (B) 65 μM rhodamine B and 0.1 g/L HNPs suspension in methanol with baseline corrected for HNPs absorbance, and (C) 0.1 g/L HNPs suspended in methanol. The curves in (B) are baseline corrected for HNPs absorption. (D) Averaged amount of rhodamine B sorbed onto HNPs plotted against pH for 65 μM rhodamine B and 0.1 g/L HNPs suspension in methanol. Error bars represent one standard deviation.

Solvent	[Rhodamine B] [μM]	pH	[HNP] [g/L]	$\tau_1\,[ps]$	$\tau_2\,[ps]$	$\tau_3\,[ps]$
Methanol	65	4.5	0.0	10 ± 10	1535 ± 58	10095 ± 737
Methanol	20	~6.7	0.0	< 63	644 ± 124	4900 ± 223
Water	20	~6.7	0.0	< 6	2300 ± 92	97100 ± 4410
Methanol	65	~6.7	0.0	< 18	1808 ±70	92973 ± 34600
Water	65	~6.7	0.0	< 115	1920 ± 75	2620 ± 44
Methanol	65	7	0.0	13 ± 11	685 ± 46	10372 ± 514
Methanol	65	9	0.0	4.4 ± 7.1	583 ± 20	5446 ± 139
Methanol	20	11	0.0	3 ± 3	6444 ± 745	5442 ± 386
Water	20	11	0.0	21 ± 16	4994 ± 2362	20154 ± 8364
Methanol	65	11	0.0	6 ± 5	5337 ± 1901	14057 ± 5108
Water	65	11	0.0	12 ± 20	1388 ± 132	5621 ± 554

Table 2. Average excited state relaxation time values for RhB suspensions at balanced (pH 4.5, pH 7, pH 9, pH 11) and unbalanced (pH 6.7) pH values in methanol and water. Error values are propagated uncertainties from the fit results for τ_2 and τ_3 .Error values represent one standard deviation for τ_1 .

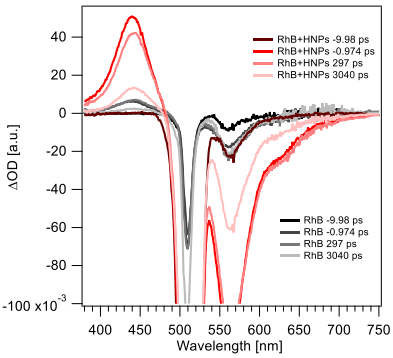

pH 4.5

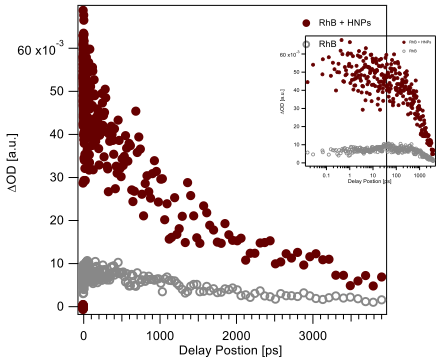

pH 4.5

Figure 2. (Top) TAS absorption spectra for 65 µM Rhodamine B with and without 0.1 g/L hematite nanoparticles suspended in methanol at pH 4.5 and at specified delay positions. **(Bottom)** Transient absorption kinetics curves for 65 µM Rhodamine B with and without 0.1 g/L hematite nanoparticles in suspension in methanol medium at pH 4.5 and at 448 nm wavelength.

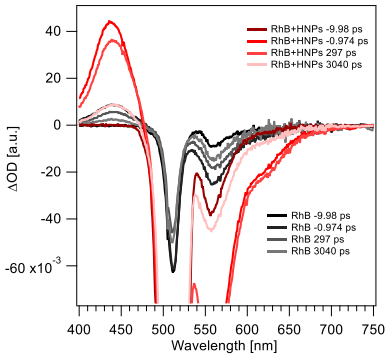

pH 7

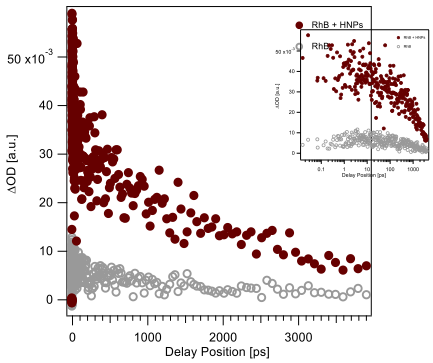

pH 7

Figure 3. (Top) TAS absorption spectra for 65 µM Rhodamine B with and without 0.1 g/L hematite nanoparticles suspended in methanol at pH 7 and at specified delay positions. **(Bottom)** Transient absorption kinetics curves for 65 µM Rhodamine B with and without 0.1 g/L hematite nanoparticles in suspension in methanol medium at pH 7 and at 448 nm wavelength.

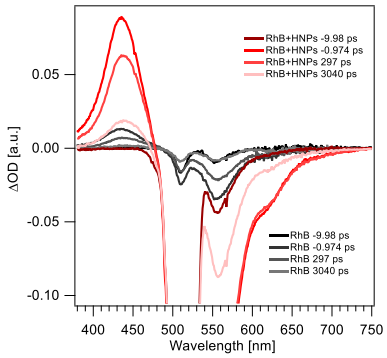

pH 9

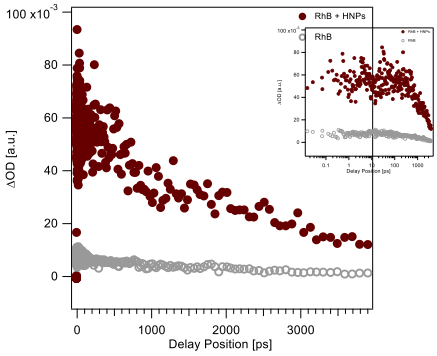

pH 9

Figure 4. (Top) TAS absorption spectra for 65 µM Rhodamine B with and without 0.1 g/L hematite nanoparticles suspended in methanol at pH 9 and at specified delay positions. **(Bottom)** Transient absorption kinetics for 65 µM Rhodamine B with and without 0.1 g/L hematite nanoparticles in suspension in methanol medium at pH 9 and at 448 nm wavelength.

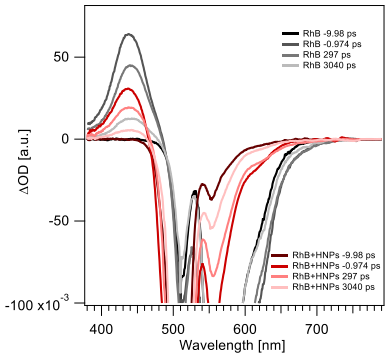

pH 11

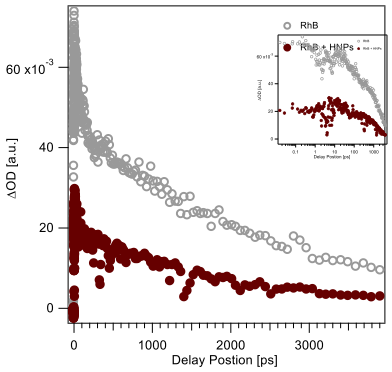

pH 11

Figure 5. (**Top**) Transient absorption spectra for 65 µM Rhodamine B with and without 0.1 g/L hematite nanoparticles suspended in methanol at pH 11 and different delay times. (**Bottom**) Transient absorption kinetics for 65 µM Rhodamine B with and without 0.1 g/L hematite nanoparticles in suspension in methanol medium at pH 11 at 448 nm wavelength.

Solvent	[Rhodamine B] [μM]	pH	[HNP] [g/L]	$\tau_1\,[ps]$	$\tau_2\,[ps]$	$\tau_3\,[ps]$
Methanol	65	4.5	0.0	10 ± 10	1535 ± 58	10095 ± 737
Methanol	65	4.5	0.1	7 ± 5	2582 ± 244	11648 ± 9464
Methanol	65	7	0.0	13 ± 11	685 ± 46	10372 ± 514
Methanol	65	7	0.1	2.5 ± 1.6	1363 ± 70	68597 ± 8116
Methanol	65	9	0.0	4.4 ± 7.1	583 ± 20	5446 ± 139
Methanol	65	9	0.1	9 ± 7	1171 ± 42	49445 ± 4883
Methanol	65	11	0.0	6 ± 5	5337 ± 1901	14057 ± 5108
Methanol	65	11	0.1	1.3 ± 0.6	4863 ± 1190	3433 ± 1023

Table 3. Average excited state relaxation time values for RhB and RhB+HNPs suspensions at varying pH values. Error values are propagated uncertainties from the fit results for τ_2 and τ_3 .Error values represent one standard deviation for τ_1 .

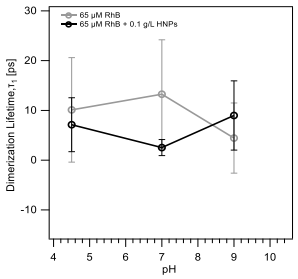

A

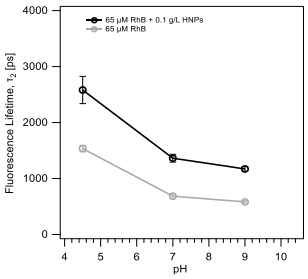

B

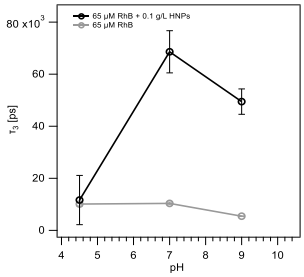

C

Figure 6. Average **(A)** dimer's excited state lifetime, τ_1, **(B)** fluorescence lifetime, τ_2, and **(C)** intersystem crossing lifetime, τ_3, plotted against pH for 65 μM rhodamine B (grey) in methanol and 65 μM rhodamine B and 0.1 g/L HNPs (black) suspension in methanol. Error bars represent one standard deviation in Fig. 5A due to huge uncertainties associated with τ_1 from the global fits. Error bars in Figs. 5B and 5C are the propagated uncertainties from global fitting results.

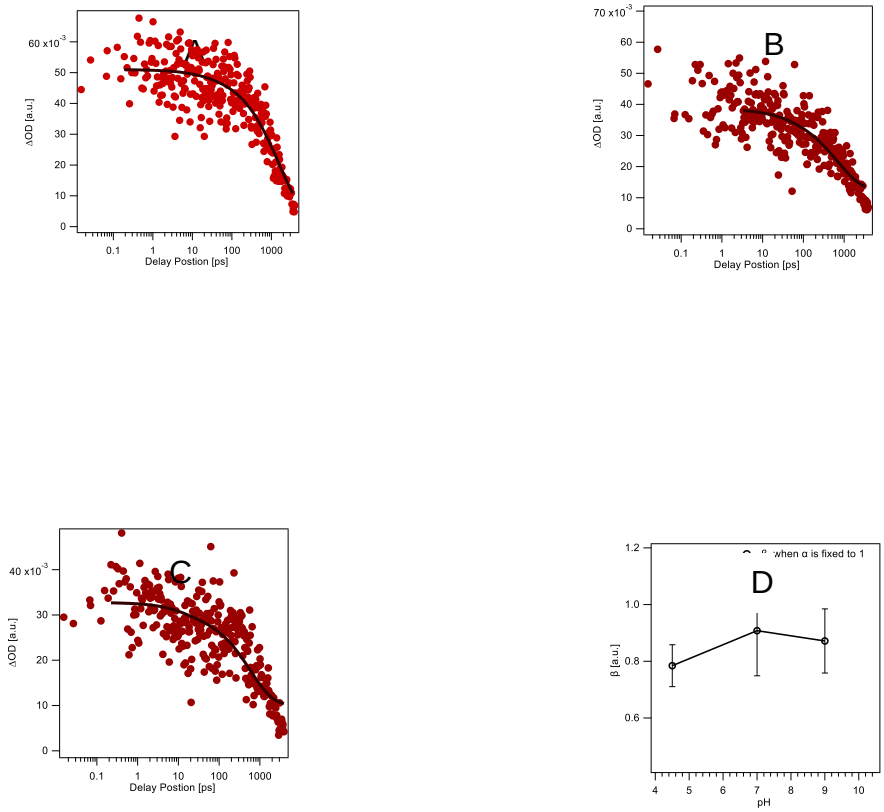

Figure 7. Transient absorption kinetics curves recorded at 448 nm for 65 µM Rhodamine B with 0.1 g/L hematite nanoparticles in suspension in methanol medium at **(A)** pH 4.5, **(B)** pH 7, and **(C)** pH 9 fitted to a stretched biexponential $[\Delta OD(t) = \Delta OD_0 + A_1 e^{-\left\{\frac{(t)}{\tau_1}\right\}^1} + A_2 e^{-\left\{\frac{(t)}{\tau_2}\right\}^\beta}]$ Here the stretching factor, α for τ_1 is set to 1 for all three pH values during fitting since τ_1 (dimer's excited state lifetime) does not change after HNPs inclusion. **(D)** Stretching parameter associated with τ_2 - fluorescence lifetime (β) plotted against pH for 65 µM

References

1. D. Buerge-Weirich and B. Sulzberger, Formation of Cu (I) in estuarine and marine waters: application of a new solid-phase extraction method to measure Cu (I), *Environ. Sci. Technol.*, 2004, **38**, 1843-1848.
2. L. Emmenegger, D. W. King, L. Sigg and B. Sulzberger, Oxidation kinetics of Fe (II) in a eutrophic Swiss lake, *Environ. Sci. Technol.*, 1998, **32**, 2990-2996.
3. W. Sunda, S. Huntsman and G. Harvey, Photoreduction of manganese oxides in seawater and its geochemical and biological implications, *Nature*, 1983, **301**, 234-236.
4. K. Sivula, F. Le Formal and M. Grätzel, Solar Water Splitting: Progress Using Hematite (α-Fe2O3) Photoelectrodes, *ChemSusChem*, 2011, **4**, 432-449.
5. K. L. Hardee and A. J. Bard, Semiconductor Electrodes: V . The Application of Chemically Vapor Deposited Iron Oxide Films to Photosensitized Electrolysis, *J. Electrochem. Soc.*, 1976, **123**, 1024-1026.
6. R. K. Quinn, R. D. Nasby and R. J. Baughman, Photoassisted electrolysis of water using single crystal α-Fe2O3 anodes, *Mater. Res. Bull.*, 1976, **11**, 1011-1017.
7. C. Lohaus, A. Klein and W. Jaegermann, Limitation of Fermi level shifts by polaron defect states in hematite photoelectrodes, *Nat. Commun.*, 2018, **9**, 4309.
8. B. Gilbert, C. Frandsen, E. R. Maxey and D. M. Sherman, Band-gap measurements of bulk and nanoscale hematite by soft x-ray spectroscopy, *Phys. Rev. B*, 2009, **79**, 035108.
9. A. H. Morrish, *Canted antiferromagnetism: hematite*, World Scientific, 1994.
10. R. M. Cornell and U. Schwertmann, *The Iron Oxides: Structures, Properties, Reactions, Occurrences and Uses*, 2003.
11. D. K. Zhong, J. Sun, H. Inumaru and D. R. Gamelin, Solar Water Oxidation by Composite Catalyst/α-Fe2O3 Photoanodes, *J. Am. Chem. Soc.*, 2009, **131**, 6086-6087.
12. A. G. Tamirat, J. Rick, A. A. Dubale, W.-N. Su and B.-J. Hwang, Using hematite for photoelectrochemical water splitting: a review of current progress and challenges, *Nanoscale Horiz.*, 2016, **1**, 243-267.
13. F. Bødker, M. F. Hansen, C. B. Koch, K. Lefmann and S. Mørup, Magnetic properties of hematite nanoparticles, *Phys. Rev. B*, 2000, **61**, 6826-6838.
14. J. Y. Kim, G. Magesh, D. H. Youn, J.-W. Jang, J. Kubota, K. Domen and J. S. Lee, Single-crystalline, wormlike hematite photoanodes for efficient solar water splitting, *Sci. Rep.*, 2013, **3**, 2681.
15. F. Li, X. Li, X. Li, T. Liu and J. Dong, Heterogeneous photodegradation of bisphenol A with iron oxides and oxalate in aqueous solution, *J. Colloid Interface Sci.*, 2007, **311**, 481-490.
16. M. Huang, W. Xiang, T. Zhou, J. Mao, X. Wu and X. Guo, The critical role of the surface iron-oxalate complexing species in determining photochemical degradation of norfloxacin using different iron oxides, *Sci. Total Environ.*, 2019, **697**, 134220.
17. S. Belaidi, L. Mammeri, H. Mechakra, W. Remache, K. Benhamouda, S. Larouk, M. Kribeche and T. Sehili, UV and solar light induced natural iron oxide activation: characterization and photocatalytic degradation of organic compounds, *Int. J. Chem. React. Eng.*, 2019, **17**.
18. M. E. A. Kribéche, H. Mechakra, T. Sehili and S. Brosillon, Oxidative photodegradation of herbicide fenuron in aqueous solution by natural iron oxide α-Fe2O3, influence of polycarboxylic acids, *Environ. Technol.*, 2016, **37**, 172-182.

19. F. M. Morel, A. Kustka and Y. Shaked, The role of unchelated Fe in the iron nutrition of phytoplankton, *Limnol. Oceanogr.* 2008, **53**, 400-404.
20. Y. Shaked and H. Lis, Disassembling iron availability to phytoplankton, *Front. Microbiol.*, 2012, **3**, 123.
21. R. M. Boiteau, D. R. Mende, N. J. Hawco, M. R. McIlvin, J. N. Fitzsimmons, M. A. Saito, P. N. Sedwick, E. F. DeLong and D. J. Repeta, Siderophore-based microbial adaptations to iron scarcity across the eastern Pacific Ocean, *Proc. Natl. Acad. Sci.*, 2016, **113**, 14237-14242.
22. R. F. Anderson, GEOTRACES: Accelerating research on the marine biogeochemical cycles of trace elements and their isotopes, *Ann. Rev. Mar. Sci.*, 2020, **12**, 49-85.
23. J. A. Howitt, D. S. Baldwin, G. N. Rees and B. T. Hart, Photodegradation, interaction with iron oxides and bioavailability of dissolved organic matter from forested floodplain sources, *Mar. Freshw. Res.*, 2008, **59**, 780-791.
24. A. M. Vindedahl, J. H. Strehlau, W. A. Arnold and R. L. J. E. S. N. Penn, Organic matter and iron oxide nanoparticles: aggregation, interactions, and reactivity, *Environ. Sci. Nano*, 2016, **3**, 494-505.
25. K. Mopper and X. L. Zhou, Hydroxyl Radical Photoproduction in the Sea and Its Potential Impact on Marine Processes, *Science*, 1990, **250**, 661-664.
26. H. H. Wu, J. J. Yin, W. G. Wamer, M. Y. Zeng and Y. M. Lo, Reactive oxygen species-related activities of nano-iron metal and nano-iron oxides, *J Food Drug Anal*, 2014, **22**, 86-94.
27. S. Gligorovski, R. Strekowski, S. Barbati and D. Vione, Environmental Implications of Hydroxyl Radicals (center dot OH), *Chem. Rev.*, 2015, **115**, 13051-13092.
28. L. Demarchis, M. Minella, R. Nistico, V. Maurino, C. Minero and D. Vione, Photo-Fenton reaction in the presence of morphologically controlled hematite as iron source, *J Photochem. Photobio. A*, 2015, **307**, 99-107.
29. K. Mopper and X. Zhou, Hydroxyl radical photoproduction in the sea and its potential impact on marine processes, *Sci.*, 1990, **250**, 661-664.
30. H. Wu, J.-J. Yin, W. G. Wamer, M. Zeng, Y. M. J. J. o. F. Lo and D. Analysis, Reactive oxygen species-related activities of nano-iron metal and nano-iron oxides, *J. Food Drug Anal.*, 2014, **22**, 86-94.
31. S. Gligorovski, R. Strekowski, S. Barbati and D. Vione, Environmental implications of hydroxyl radicals (• OH), *Chem. Rev.*, 2015, **115**, 13051-13092.
32. L. Demarchis, M. Minella, R. Nisticò, V. Maurino, C. Minero and D. Vione, Photo–Fenton reaction in the presence of morphologically controlled hematite as iron source, *J. Photochem. Photobiol. A: Chem.*, 2015, **307**, 99-107.
33. W. Stumm and B. Sulzberger, The cycling of iron in natural environments: Considerations based on laboratory studies of heterogeneous redox processes, *Geochim. Cosmochim. Acta*, 1992, **56**, 3233.
34. P. Borer, B. Sulzberger, S. J. Hug, S. M. Kraemer and R. Kretzschmar, Photoreductive dissolution of iron (III)(hydr) oxides in the absence and presence of organic ligands: Experimental studies and kinetic modeling, *Environ. Sci. Technol.*, 2009, **43**, 1864-1870.
35. K. Kuma, S. Nakabayashi and K. J. W. R. Matsunaga, Photoreduction of Fe (III) by hydroxycarboxylic acids in seawater, *Water Res.*, 1995, **29**, 1559-1569.
36. B. Sulzberger and H. Laubscher, Reactivity of various types of iron (III)(hydr) oxides towards light-induced dissolution, *Mar. Chem.*, 1995, **50**, 103-115.

37. X. Huang, Y. Chen, E. Walter, M. Zong, Y. Wang, X. Zhang, O. Qafoku, Z. Wang and K. M. Rosso, Facet-Specific Photocatalytic Degradation of Organics by Heterogeneous Fenton Chemistry on Hematite Nanoparticles, *Environ. Sci. Technol.*, 2019, **53**, 10197-10207.
38. C. S. Ahart, K. M. Rosso and J. Blumberger, Electron and Hole Mobilities in Bulk Hematite from Spin-Constrained Density Functional Theory, *J. Am. Chem. Soc.*, 2022, **144**, 4623-4632.
39. V. Alexandrov and K. M. Rosso, Electron transport in pure and substituted iron oxyhydroxides by small-polaron migration, *J. Chem. Phys.*, 2014, **140**, 234701.
40. K. M. Rosso, D. M. A. Smith and M. Dupuis, An ab initio model of electron transport in hematite (α-Fe2O3) basal planes, *J. Chem. Phys.*, 2003, **118**, 6455-6466.
41. C. S. Ahart, J. Blumberger and K. M. Rosso, Polaronic structure of excess electrons and holes for a series of bulk iron oxides, *Phys. Chem. Chem. Phys.*, 2020, **22**, 10699-10709.
42. S. Kerisit and K. M. Rosso, Kinetic Monte Carlo model of charge transport in hematite (α-Fe2O3), *J. Chem. Phys.*, 2007, **127**, 124706.
43. J. L. Shelton and K. E. J. a. p. a. Knowles, Polaronic Optical Transitions in Hematite (α-Fe2O3) Revealed by First-Principles Electron-Phonon Coupling, 2022.
44. J. E. Katz, B. Gilbert, X. Zhang, K. Attenkofer, R. W. Falcone and G. A. Waychunas, Observation of Transient Iron(II) Formation in Dye-Sensitized Iron Oxide Nanoparticles by Time-Resolved X-ray Spectroscopy, *J. Phys. Chem. Lett.*, 2010, **1**, 1372-1376.
45. J. E. Katz, X. Zhang, K. Attenkofer, K. W. Chapman, C. Frandsen, P. Zarzycki, K. M. Rosso, R. W. Falcone, G. A. Waychunas and B. Gilbert, Electron small polarons and their mobility in iron (oxyhydr)oxide nanoparticles, *Sci.*, 2012, **337**, 1200-1203.
46. P. Mulvaney, V. Swayambunathan, F. Grieser and D. Meisel, Dynamics of interfacial charge transfer in iron(III) oxide colloids, *J. Phys. Chem.*, 1988, **92**, 6732.
47. J. K. Leland and A. J. Bard, Photochemistry of colloidal semiconducting iron oxide polymorphs, *J. Phys. Chem.*, 1987, **91**, 5076-5083.
48. J. A. Soltis, A. M. Schwartzberg, P. Zarzycki, R. L. Penn, K. M. Rosso and B. Gilbert, Electron Mobility and Trapping in Ferrihydrite Nanoparticles, *ACS Earth Space Chem.*, 2017, **1**, 216-226.
49. A. S. M. Ismail, Y. Uemura, S. H. Park, S. Kwon, M. Kim, H. Elnaggar, F. Frati, Y. Niwa, H. Wadati, Y. Hirata, Y. Zhang, K. Yamagami, S. Yamamoto, I. Matsuda, U. Halisdemir, G. Koster, B. M. Weckhuysen and F. M. F. de Groot, Direct observation of the electronic states of photoexcited hematite with ultrafast 2p3d X-ray absorption spectroscopy and resonant inelastic X-ray scattering, *Phys. Chem. Chem. Phys.*, 2020, **22**, 2685-2692.
50. N. J. Cherepy, D. B. Liston, J. A. Lovejoy, H. Deng and J. Z. Zhang, Ultrafast Studies of Photoexcited Electron Dynamics in γ- and α-Fe2O3 Semiconductor Nanoparticles, *J. Phys. Chem. B*, 1998, **102**, 770-776.
51. C. Bressler, C. Milne, V. T. Pham, A. ElNahhas, R. M. van der Veen, W. Gawelda, S. Johnson, P. Beaud, D. Grolimund, M. Kaiser, C. N. Borca, G. Ingold, R. Abela and M. Chergui, Femtosecond XANES Study of the Light-Induced Spin Crossover Dynamics in an Iron(II) Complex, *Sci.*, 2009, **323**, 489.
52. S. S. Cai and J. D. Stark, Evaluation of five fluorescent dyes and triethyl phosphate as atmospheric tracers of agricultural sprays, *J. Environ. Sci. Health, B*, 1997, **32**, 969-983.
53. M. Beija, C. A. M. Afonso and J. M. G. Martinho, Synthesis and applications of Rhodamine derivatives as fluorescent probes, *Chem. Soc. Rev.*, 2009, **38**, 2410-2433.

54. D. Catone, P. O'Keeffe, M. Satta, A. Paladini, A. Ciavardini, F. Toschi, S. Turchini and L. Avaldi, A combined theoretical and experimental study of the ultrafast photophysics of Rhodamine B, *Mol. Phys.*, 2018, **116**, 2162-2171.
55. A. S. Kristoffersen, S. R. Erga, B. Hamre and Ø. Frette, Testing Fluorescence Lifetime Standards using Two-Photon Excitation and Time-Domain Instrumentation: Rhodamine B, Coumarin 6 and Lucifer Yellow, *J. Fluoresc.*, 2014, **24**, 1015-1024.
56. R. J. Vázquez, H. Kim, P. M. Zimmerman and T. Goodson, Using ultra-fast spectroscopy to probe the excited state dynamics of a reported highly efficient thermally activated delayed fluorescence chromophore, *J. Mater. Chem. C*, 2019, **7**, 4210-4221.
57. X.-F. Zhang, Y. Zhang and L. Liu, Fluorescence lifetimes and quantum yields of ten rhodamine derivatives: Structural effect on emission mechanism in different solvents, *J. Lumin.*, 2014, **145**, 448-453.
58. M. Savarese, A. Aliberti, I. De Santo, E. Battista, F. Causa, P. A. Netti and N. Rega, Fluorescence Lifetimes and Quantum Yields of Rhodamine Derivatives: New Insights from Theory and Experiment, *J. Phys. Chem. A*, 2012, **116**, 7491-7497.
59. D. Magde, G. E. Rojas and P. G. Seybold, Solvent Dependence of the Fluorescence Lifetimes of Xanthene Dyes, *Photochem. Photobiol.*, 1999, **70**, 737-744.
60. U. K. A. Klein and F. W. Hafner, A new dual fluorescence with rhodamine B lactone, *Chem. Phys. Lett.*, 1976, **43**, 141-145.
61. F. L. Arbeloa, P. R. Ojeda and I. L. Arbeloa, Flourescence self-quenching of the molecular forms of Rhodamine B in aqueous and ethanolic solutions, *J. Lumin.*, 1989, **44**, 105-112.
62. N. K. M. N. Srinivas, S. V. Rao and D. N. Rao, Saturable and reverse saturable absorption of Rhodamine B in methanol and water, *J. Opt. Soc. Am. B*, 2003, **20**, 2470-2479.
63. S. Venugopal Rao, N. K. M. Naga Srinivas and D. Narayana Rao, Nonlinear absorption and excited state dynamics in Rhodamine B studied using Z-scan and degenerate four wave mixing techniques, *Chem. Phys. Lett.*, 2002, **361**, 439-445.
64. I. L. Arbeloa and K. K. Rohatgi-Mukherjee, Solvent effects on the photophysics of the molecular forms of rhodamine B. Internal conversion mechanism, *Chem. Phys. Lett.*, 1986, **129**, 607-614.
65. F. López Arbeloa, T. López Arbeloa, M. Tapia Estévez and I. López Arbeloa, Photophysics of rhodamines: molecular structure and solvent effects, *J. Phys. Chem.*, 1991, **95**, 2203-2208.
66. J. Nelson, Continuous-time random-walk model of electron transport in nanocrystalline TiO2 electrodes, *Phys. Rev. B: Condens. Matter Mater. Phys.*, 1999, **59**, 15374.
67. S. A. Theofanidis, V. V. Galvita, C. Konstantopoulos, H. Poelman and G. B. Marin, Fe-Based Nano-Materials in Catalysis, *Materials*, 2018, **11**.
68. P. Tartaj, M. P. Morales, T. Gonzalez-Carreño, S. Veintemillas-Verdaguer and C. J. Serna, The Iron Oxides Strike Back: From Biomedical Applications to Energy Storage Devices and Photoelectrochemical Water Splitting, *Adv. Mater.*, 2011, **23**, 5243-5249.
69. P. Xu, G. M. Zeng, D. L. Huang, C. L. Feng, S. Hu, M. H. Zhao, C. Lai, Z. Wei, C. Huang, G. X. Xie and Z. F. Liu, Use of iron oxide nanomaterials in wastewater treatment: A review, *Sci. Total Environ.*, 2012, **424**, 1-10.
70. L. Chen, X. Yang, J. Chen, J. Liu, H. Wu, H. Zhan, C. Liang and M. Wu, Continuous Shape- and Spectroscopy-Tuning of Hematite Nanocrystals, *Inorg. Chem.*, 2010, **49**, 8411-8420.

71. J. J. Snellenburg, S. P. Laptenok, R. Seger, K. M. Mullen and I. H. van Stokkum, Glotaran: A Java-based graphical user interface for the R package TIMP, *J. Stat. Softw.*, 2012.
72. D. C. Johnston, Stretched exponential relaxation arising from a continuous sum of exponential decays, *Phys. Rev. B*, 2006, **74**, 184430.
73. S. R. Pendlebury, M. Barroso, A. J. Cowan, K. Sivula, J. Tang, M. Grätzel, D. Klug and J. R. Durrant, Dynamics of photogenerated holes in nanocrystalline α-Fe_2O_3 electrodes for water oxidation probed by transient absorption spectroscopy, *Chem. Commun.*, 2010, **47**, 716-718.
74. C.-y. Wang, C. Böttcher, D. W. Bahnemann and J. K. Dohrmann, A comparative study of nanometer sized Fe (III)-doped TiO 2 photocatalysts: synthesis, characterization and activity, *J. Mater. Chem.*, 2003, **13**, 2322-2329.
75. X. Xue, K. Hanna and N. Deng, Fenton-like oxidation of Rhodamine B in the presence of two types of iron (II, III) oxide, *J. Hazard. Mater.*, 2009, **166**, 407-414.
76. K. Hanna, Sorption of two aromatic acids onto iron oxides: Experimental study and modeling, *J. Colloid Interface Sci.*, 2007, **309**, 419-428.
77. I. L. Arbeloa and P. R. Ojeda, Molecular forms of rhodamine B, *Chem. Phys. Lett.*, 1981, **79**, 347-350.
78. J. Karpiuk and Z. R. Grabowski, Transient spectroscopy of rhodamine B evidence for a new intermediate, *AIP Conf. Proc.*, 1996, **364**, 91-98.
79. G. Sharifzade, A. Asghari and M. Rajabi, Highly effective adsorption of xanthene dyes (rhodamine B and erythrosine B) from aqueous solutions onto lemon citrus peel active carbon: characterization, resolving analysis, optimization and mechanistic studies, *RSC Advances*, 2017, **7**, 5362-5371.
80. F. Motahari, M. R. Mozdianfard and M. Salavati-Niasari, Synthesis and adsorption studies of NiO nanoparticles in the presence of H2acacen ligand, for removing Rhodamine B in wastewater treatment, *Process Saf. Environ. Prot.*, 2015, **93**, 282-292.
81. L. A. Ramírez-Montoya, V. Hernández-Montoya and M. A. Montes-Morán, Optimizing the preparation of carbonaceous adsorbents for the selective removal of textile dyes by using Taguchi methodology, *J. Anal. Appl. Pyrolysis*, 2014, **109**, 9-20.
82. X. Zhou, Q. Xu, W. Lei, T. Zhang, X. Qi, G. Liu, K. Deng and J. Yu, Origin of Tunable Photocatalytic Selectivity of Well-Defined α-Fe2O3 Nanocrystals, *Small*, 2014, **10**, 674-679.
83. P. Zarzycki, S. Chatman, T. Preočanin and K. M. Rosso, Electrostatic Potential of Specific Mineral Faces, *Langmuir*, 2011, **27**, 7986-7990.
84. S. Chatman, P. Zarzycki and K. M. Rosso, Surface potentials of (001), (012), (113) hematite (α-Fe2O3) crystal faces in aqueous solution, *Phys. Chem. Chem. Phys.*, 2013, **15**, 13911-13921.
85. Y. Wang, P. Persson, F. M. Michel and G. E. Brown, Comparison of isoelectric points of single-crystal and polycrystalline α-Al2O3 and α-Fe2O3 surfaces *Am. Mineral.*, 2016, **101**, 2248-2259.
86. Z. Shen, Z. Zhang, T. Li, Q. Yao, T. Zhang and W. Chen, Facet-Dependent Adsorption and Fractionation of Natural Organic Matter on Crystalline Metal Oxide Nanoparticles, *Environ. Sci. Technol.*, 2020, **54**, 8622-8631.
87. M. J. Snare, F. E. Treloar, K. P. Ghiggino and P. J. Thistlethwaite, The photophysics of rhodamine B, *J. Photochem.*, 1982, **18**, 335-346.

88. X. Wang, O. Ozdemir, M. A. Hampton, A. V. Nguyen and D. D. Do, The effect of zeolite treatment by acids on sodium adsorption ratio of coal seam gas water, *Water Res.*, 2012, **46**, 5247-5254.
89. R. Zhang, M. Hummelgård, G. Lv and H. Olin, Real time monitoring of the drug release of rhodamine B on graphene oxide, *Carbon*, 2011, **49**, 1126-1132.
90. C. Namasivayam, N. Muniasamy, K. Gayatri, M. Rani and K. Ranganathan, Removal of dyes from aqueous solutions by cellulosic waste orange peel, *Bioresour. Technol.*, 1996, **57**, 37-43.
91. A. L. Smirl, J. B. Clark, E. W. V. Stryland and B. R. Russell, Population and rotational kinetics of the rhodamine B monomer and dimer: Picosecond transient spectrometry, *J. Chem. Phys.*, 1982, **77**, 631-640.
92. R. Menzel and E. Thiel, Intersystem crossing rate constants of rhodamine dyes: influence of the amino-group substitution, *Chem. Phys. Lett.*, 1998, **291**, 237-243.
93. V. Nadtochenko, N. Denisov, V. Y. Gak, F. Gostev, A. Titov, O. Sarkisov and V. J. R. c. b. Nikandrov, Femtosecond relaxation of photoexcited states in nanosized semiconductor particles of iron oxides, *Russ. Chem. Bull.*, 2002, **51**, 457-461.
94. G. Xiong, A. G. Joly, G. P. Holtom, C. Wang, D. E. McCready, K. M. Beck and W. P. Hess, Excited Carrier Dynamics of α-Cr2O3/α-Fe2O3 Core−Shell Nanostructures, *J. Phys. Chem. B*, 2006, **110**, 16937-16940.
95. A. G. Joly, J. R. Williams, S. A. Chambers, G. Xiong, W. P. Hess and D. M. Laman, Carrier dynamics in α-Fe2O3 (0001) thin films and single crystals probed by femtosecond transient absorption and reflectivity, *J. Appl. Phys.*, 2006, **99**, 053521.
96. H. M. Fan, G. J. You, Y. Li, Z. Zheng, H. R. Tan, Z. X. Shen, S. H. Tang and Y. P. Feng, Shape-Controlled Synthesis of Single-Crystalline Fe2O3 Hollow Nanocrystals and Their Tunable Optical Properties, *J. Phys. Chem. C*, 2009, **113**, 9928-9935.
97. S. Sorenson, E. Driscoll, S. Haghighat and J. M. Dawlaty, Ultrafast Carrier Dynamics in Hematite Films: The Role of Photoexcited Electrons in the Transient Optical Response, *J. Phys. Chem. C*, 2014, **118**, 23621-23626.
98. S. R. Pendlebury, M. Barroso, A. J. Cowan, K. Sivula, J. Tang, M. Grätzel, D. Klug and J. R. Durrant, Dynamics of photogenerated holes in nanocrystalline α-Fe2O3 electrodes for water oxidation probed by transient absorption spectroscopy, *Chem. Commun.*, 2011, **47**, 716-718.
99. B. Gilbert, J. E. Katz, N. Huse, X. Zhang, C. Frandsen, R. W. Falcone and G. A. Waychunas, Ultrafast electron and energy transfer in dye-sensitized iron oxide and oxyhydroxide nanoparticles, *Phys. Chem. Chem. Phys.*, 2013, **15**, 17303.
100. P. Zarzycki and K. M. Rosso, Surface Charge Effects on Fe(II) Sorption and Oxidation at (110) Goethite Surfaces, *J. Phys. Chem. C*, 2018, **122**, 10059-10066.